

Probing a regular orbit with spectral dynamics

Y. Copin¹ [★], H.S. Zhao², P.T. de Zeeuw²

¹Centre de Recherche Astronomique de Lyon [†], Observatoire de Lyon, 69561 Saint-Genis-Laval cedex, France

²Sterrewacht Leiden, Niels Bohrweg 2, 2333 CA, Leiden, The Netherlands

Accepted; Received; In original form

ABSTRACT

We have extended the spectral dynamics formalism introduced by Binney & Spergel, and have implemented a semi-analytic method to represent regular orbits in any potential, making full use of their regularity. We use the spectral analysis code of Carpintero & Aguilar to determine the nature of an orbit (irregular, regular, resonant, periodic) from a short-time numerical integration. If the orbit is regular, we approximate it by a truncated Fourier time series of a few tens of terms per coordinate. Switching to a description in action-angle variables, this corresponds to a reconstruction of the underlying invariant torus. We then relate the uniform distribution of a regular orbit on its torus to the non-uniform distribution in the space of observables by a simple Jacobian transformation between the two sets of coordinates. This allows us to compute, in a cell-independent way, all the physical quantities needed in the study of the orbit, including the density and in the line-of-sight velocity distribution, with much increased accuracy. The resulting flexibility in the determination of the orbital properties, and the drastic reduction of storage space for the orbit library, provide a significant improvement in the practical application of Schwarzschild's orbit superposition method for constructing galaxy models. We test and apply our method to two-dimensional orbits in elongated discs, and to the meridional motion in axisymmetric potentials, and show that for a given accuracy, the spectral dynamics formalism requires an order of magnitude fewer computations than the more traditional approaches.

Key words: galaxies: kinematics and dynamics – celestial mechanics, stellar dynamics

1 INTRODUCTION

In the construction of dynamical models for galaxies by Schwarzschild's (1979) method, one tries to match the density distribution and the photometric and kinematic observations with weighted contributions of individual orbits (e.g., Rix et al. 1997; Cretton et al. 1999). Therefore, the method requires the precise knowledge of the intrinsic properties of the orbits, such as the density and the line-of-sight velocity distributions (LOSVD's). The traditional method for computing the orbital properties is to integrate the equations of motion by numerical means. Then the spatial density distribution of the orbit follows from calculating the fraction of time spent in each cell of a grid in configuration space after a sufficiently long integration period. Other properties follow by considering similar grids in phase-space. This method can be visualized as simply marching along the orbit, and dropping balls in a grid of buckets at regular

time intervals. It is conceptually similar to a Monte-Carlo integration, and can be applied to any orbit. However, this approach does not take advantage of the regular behavior of many orbits in the potentials relevant for galaxies: it simply treats the regular orbital motion as a structureless collection of independent points in phase-space.

The motion in a regular orbit is quasi-periodic, and can be expressed as a Fourier series expansion in action-angle variables. This series expansion represents the underlying invariant orbital torus (e.g., Arnold 1989), and can be reconstructed from a normal orbit integration (Binney & Spergel 1982, 1984), or from generating functions (McGill & Binney 1990, Binney & Kumar 1993, Kaasalainen & Binney 1994, Kaasalainen 1994). It is also possible to integrate the orbit directly in the angle variables (Ratcliff, Chang & Schwarzschild 1984), although published applications have been restricted to two-dimensional motion. Laskar (1993) introduced the so-called frequency map analysis to study the nature of orbits. This has been used to study orbits in galactic potentials (Papaphilippou & Laskar 1996, 1998; Val-luri & Merritt 1998). Carpintero & Aguilar (1998, hereafter CA98) developed a fully automated technique to classify or-

[★] E-mail: ycopic@obs.univ-lyon1.fr

[†] UMR CNRS 5574, École normale supérieure de Lyon - Université Claude Bernard Lyon I

bits based on the commensurability of the peak frequencies in the Fourier spectra of the orbit.

In this paper we extend this previous work as follows. From a standard numerical integration of the orbit over a few hundred orbital periods, and after a detailed spectral analysis based on the method of CA98, we obtain a semi-analytic expression for the orbit. This can be considered as fitting the underlying orbital torus to the results of a short numerical integration, and so obtaining an approximate expression for the orbit valid for all time (i.e., fully phase-mixed). It is then straightforward to derive all the required orbital properties, including the density in configuration space and the LOSVD's, with high precision, and we describe in detail how to do this. While there are many papers on orbital tori reconstruction in the literature, we are not aware of any published formalism for projecting the tori to observable space to get the LOSVD of an orbit. Here we implement our method on two-dimensional integrable and non-integrable potentials, and compare the results with traditional straight numerical integrations. We also show how to generalize the results to axisymmetric three-dimensional potential.

This paper is organized as follows. After reviewing some basic results of spectral dynamics in §2, we present the extended formalism in §3. In §4 we test the formalism on a two-dimensional separable (Stäckel) potential, and then apply it to Binney's logarithmic potential. We describe the application to the motion in the meridional plane of an axisymmetric potential in §5, and summarize our conclusions in §6.

2 INTRODUCTION TO SPECTRAL DYNAMICS

For the convenience of the general reader, we here summarize some results on the structure of phase-space, and introduce the terminology and notations of action-angle description of orbits.

2.1 Phase-space structure, action-angle variables and base frequencies

In an n -dimensional potential (cases of interest are $n = 2$ or 3), an orbit can be characterized according to its m integrals. In a time-independent potential, the energy is a conserved quantity and is always an integral for an orbit, leading to $m \geq 1$. When the orbital motion in phase-space (of dimension $2n$) is constrained by the conservation of m integrals of motion, the orbital manifold on which the orbit evolves has dimension $2n - m$. The orbit is said to be *regular* if $m \geq n$, and then travels on a manifold of dimension $\leq n$; otherwise ($m < n$), the orbit is said to be *irregular* (or *chaotic*), and move in a region of phase-space of dimension $> n$ (but still $\leq 2n - 1$).

In the special case $m = n$, the orbital manifold of a bound orbit is topologically equivalent to an n -torus, the *invariant torus*, embedded in phase-space (e.g., Arnold 1989; see Fig. 1), and the orbital motion is *quasi-periodic*. Not being further constrained by additional integrals of motion, the trajectory is *dense* (or *ergodic*) on the torus, and the orbit is said to be *open*. On the other hand, if $m > n$, the orbit is

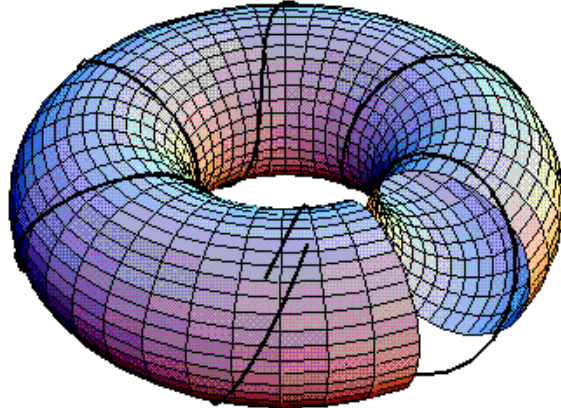


Figure 1. A regular open orbit spiraling on its invariant torus.

further constrained, and will not cover densely its torus even after infinite time. This happens when there exist resonances between the fundamental frequencies of two or more angle variables describing the orbit (cf. following section). Thus, we speak of *non-resonant* ($m = n$) and *resonant* ($m > n$) orbital tori; only the former form a set of non-zero measure in phase-space. If the orbit is *fully resonant*, i.e., $m = 2n - 1$, it closes on itself only after a finite number of turns around its torus: such an orbit is *periodic*.

A regular orbit is confined to its invariant n -torus, so we can look for canonical coordinates (\mathbf{Q}, \mathbf{P}) adapted to the torus geometry, such that the momenta \mathbf{P} are constant on the torus, and their conjugate variables \mathbf{Q} form a natural coordinate system for the region of phase-space occupied by the tori. Since these coordinates are canonical, Hamilton's equations state:

$$\dot{\mathbf{Q}} = \frac{\partial H}{\partial \mathbf{P}}, \quad \dot{\mathbf{P}} = -\frac{\partial H}{\partial \mathbf{Q}}, \quad (1)$$

where H is the Hamiltonian of the orbit. Since we want \mathbf{P} to be constant, this implies that $H = H(\mathbf{P})$, i.e., that H is cyclic in \mathbf{Q} , and thus that $\partial H / \partial \mathbf{P} = \text{cte} = \boldsymbol{\omega}$. We can therefore integrate the remaining equation of motion straightforwardly: $\mathbf{Q}(t) = \boldsymbol{\omega} t + \mathbf{Q}(0)$.

Choosing an appropriate scaling such that \mathbf{Q} is 2π -periodic, we obtain the so-called *action-angle variables*: the angles $\boldsymbol{\varphi} \equiv \mathbf{Q}$ are natural coordinates for the invariant torus, and allow one to distinguish individual points on it; the actions $\mathcal{J} \equiv \mathbf{P}$ label this torus with respect to the tori of other orbits. They can be seen as related to the different radii of the tori.

If the frequencies (actually pulsations) ω_i ($i = 1, \dots, n$) are mutually incommensurable, they are said to be the $n_{\text{BF}} = n$ *base frequencies* of the orbit; the incommensurability ensures that the orbit covers densely its torus and therefore is open. If there exist a linear commensurability between two or more ω_i , then the orbit is further constrained on the torus, and the number of incommensurable base frequencies is reduced to $n_{\text{BF}} < n$. In the extreme case, if the orbit is closed, only one base frequency remains. In the other extreme case, the base frequencies are not well-defined for irregular orbits, since these are not constrained to a n -torus; however, according to the practical definition of the base frequencies, they will be characterized by $n_{\text{BF}} > n$ (CA98).

2.2 Description of an orbit in angle variables

We now turn to the two-dimensional case, $n = 2$, and restrict ourselves to *regular open orbits*, which leads to $n_{\text{BF}} = n = 2$. The other regular orbits (with $n_{\text{BF}} < 2$) can be considered as a degenerate subset of this case, in the sense that the resonances lead to invariant tori of zero measure in phase space.

A regular open orbit in a two-dimensional potential is characterized by its two base frequencies $\omega \doteq 2\pi\nu$. The angle variables $\varphi \in [0, 2\pi[$ are then given by

$$\varphi(t) = \omega t, \quad (2)$$

where we have chosen the zero of time such that $\varphi(0) = \mathbf{0}$. We can then write the position $\mathbf{r} \equiv (x, y)$ and the velocity $\mathbf{v} \doteq \dot{\mathbf{r}}$ at time t as

$$\mathbf{r}(t) \equiv \mathbf{r}(\varphi(t)) \quad \text{and} \quad \mathbf{v}(t) \equiv \mathbf{v}(\varphi(t)). \quad (3)$$

The quasi-periodicity of the orbit allows us to write the orbital motion in a Fourier form (Binney & Spergel, 1982):

$$\begin{cases} x(t) = \sum_{l,m} X_{(l,m)} \cos(\omega_{(l,m)} t + \chi_{(l,m)}), \\ y(t) = \sum_{l,m} Y_{(l,m)} \cos(\omega_{(l,m)} t + \psi_{(l,m)}), \end{cases} \quad (4)$$

where $(l, m) \subset \mathbb{Z}^2$ are pairs of integers, $\chi_{(l,m)}$ and $\psi_{(l,m)}$ are constant phases, and the frequencies $\omega_{(l,m)}$ are linear combinations of the base frequencies:

$$\omega_{(l,m)} \equiv l\omega_1 + m\omega_2 \doteq \boldsymbol{\lambda} \cdot \boldsymbol{\omega}, \quad (5)$$

and we have used the shorthand $\boldsymbol{\lambda} \equiv (l, m)$. Alternatively we can write

$$x(t) = \sum_{\boldsymbol{\lambda}} X_{\boldsymbol{\lambda}} \cos(\boldsymbol{\lambda} \cdot \boldsymbol{\omega} t + \chi_{\boldsymbol{\lambda}}), \quad (6)$$

for the position and

$$v_x(t) = - \sum_{\boldsymbol{\lambda}} \boldsymbol{\lambda} \cdot \boldsymbol{\omega} X_{\boldsymbol{\lambda}} \sin(\boldsymbol{\lambda} \cdot \boldsymbol{\omega} t + \chi_{\boldsymbol{\lambda}}) \quad (7)$$

for the velocity, and similar expressions for $y(t)$ and $v_y(t)$.

Switching from time t to angle variables φ by means of eq. (2), we obtain the torus expression of the motion (in what we will refer to as the φ -space hereafter), in the sense that angle variables are natural coordinates for the invariant torus on which the regular orbit evolves:

$$x(\varphi) = \sum_{\boldsymbol{\lambda}} X_{\boldsymbol{\lambda}} \cos(\boldsymbol{\lambda} \cdot \boldsymbol{\varphi} + \chi_{\boldsymbol{\lambda}}), \quad (8)$$

$$v_x(\varphi) = - \sum_{\boldsymbol{\lambda}} X_{\boldsymbol{\lambda}} \boldsymbol{\lambda} \cdot \boldsymbol{\omega} \sin(\boldsymbol{\lambda} \cdot \boldsymbol{\varphi} + \chi_{\boldsymbol{\lambda}}), \quad (9)$$

and similar expressions for $y(\varphi)$ and $v_y(\varphi)$.

3 EXTENDED FORMALISM

3.1 φ -inversion

The first step for calculating the density ρ at a point $\mathbf{r}_0 = (x_0, y_0)$ in configuration space is to find the corresponding actions and angles at that point. However, while $\mathbf{r}(\varphi)$ and $\dot{\mathbf{r}}(\varphi)$ (cf. eqs (8) and (9)) are single-valued functions, the inverse functions $\varphi(\mathbf{r})$ and $\varphi(\dot{\mathbf{r}})$ are generally multi-valued. For instance, a given position \mathbf{r}_0 on the orbit corresponds in

general to a still-to-be-defined number N of solutions $\varphi_0^{(i)}$ such that:

$$\mathbf{r}(\varphi_0^{(i)}) = \mathbf{r}_0, \quad i = 1, \dots, N. \quad (10)$$

The total number N of solutions is finite (see, e.g., Fig. 4). We will refer to the N different single-valued functions involved in the definition of φ by $\varphi^{(i)}$, such that $\mathbf{r}(\varphi^{(i)})$ can be inverted.

The non-uniqueness of the solution can be understood, in the case of $\varphi(\mathbf{r})$ for instance, by the fact that an orbit usually has a finite number of ways to reach a given point \mathbf{r}_0 , either from a different part of the trajectory, or along the same part of trajectory but in different directions in a case of an orbit without a given sense of propagation (such as a box orbit). Accordingly, for a given orbit we can predict the general number of solutions N (excepting the degenerate cases) of eq. (10). Specifically, $N = 2$ for an open two-dimensional tube orbit, since the orbit can usually access a given point along two paths with a given direction of propagation imposed by the fixed sense of rotation. $N = 1$ on the boundaries of the orbit. For a flat box orbit each of the two paths through a given point can be traveled in both directions since there is no fixed sense of rotation, so that $N = 4$. On the outer boundaries of the box, degeneracy results in $N = 2$, or even $N = 1$ in the corners of the orbit, which are accessible in only one way (the one perpendicular to the zero-velocity curve; see Ollongren 1962). Each time a resonance brings two distinct parts of the orbit on top of each other, it is easy to see that the number of solutions in the zone of overlap will be doubled. For instance, we expect $N = 8$ in the zone of overlap of an open $3 : 2$ ('fish') orbit (Miralda-Escudé & Schwarzschild 1989; CA98).

3.2 Orbital density

In configuration space, we can define the orbital density ρ at point \mathbf{r}_0 by writing the mass of the orbit enclosed in the element of volume $d\tau = dx dy$ around \mathbf{r}_0 as

$$dm \doteq \rho(\mathbf{r}_0) d\tau. \quad (11)$$

Equivalently, in φ -space, we can define the density ρ_{φ} at a point φ_0 such that the mass enclosed in the element of volume $d\phi = d\varphi_1 d\varphi_2$ around φ_0 is:

$$dm' \doteq \rho_{\varphi}(\varphi_0) d\phi. \quad (12)$$

If we choose to normalize the total mass of the orbit to 1, then $\int dm = \int dm' = 1$.

An open orbit, i.e., an orbit with two incommensurable base frequencies, will eventually fill its torus uniformly, so that the density ρ_{φ} in φ -space is constant ('time averages theorem', BT87). Mass normalization then gives:

$$\rho_{\varphi} = \frac{1}{\int d\phi} = \frac{1}{(2\pi)^2}. \quad (13)$$

If the orbit is closed, i.e., the orbit has only one base frequency, all the other frequencies in eq. (4) being commensurable with it, then the time averages theorem does not apply, since the orbit is confined to a closed spiral on its torus by a new integral of motion.

Using the N single-valued functions $\varphi^{(i)}$ giving the solutions $\varphi_0^{(i)}$ of eq. (10), we can relate the element of volume $d\tau$

around the point \mathbf{r}_0 to the elements of volume $d\phi^{(i)}$ around $\varphi_0^{(i)}$:

$$d\phi^{(i)} = \left| \frac{\partial \varphi^{(i)}}{\partial \mathbf{r}} \right|_{\mathbf{r}_0} d\tau = \frac{d\tau}{J_r^{(i)}}, \quad (14)$$

where we have defined the Jacobian $J_r^{(i)}$ as in eq. (19):

$$J_r^{(i)} \doteq \left| \frac{\partial \mathbf{r}}{\partial \varphi} \right|_{\varphi_0^{(i)}}. \quad (15)$$

We can then link the density ρ to the constant density ρ_φ given by eq. (13) by properly relating eqs (11) and (12):

$$dm \equiv \sum_{i=1}^N dm^{(i)}, \quad (16)$$

with $dm^{(i)} \doteq \rho_\varphi(\varphi_0^{(i)}) d\phi^{(i)}$, since the mass lying in $d\tau$ around a given point is the sum of the masses lying in the various elements $d\phi^{(i)}$ contributing to $d\tau$. This gives:

$$dm = \frac{d\tau}{(2\pi)^2} \sum_{i=1}^N \frac{1}{J_r^{(i)}}, \quad (17)$$

which, by comparison with eq. (11), leads to the final expression:

$$\rho(\mathbf{r}_0) = \frac{1}{(2\pi)^2} \sum_{i=1}^N \frac{1}{J_r^{(i)}}, \quad (18)$$

the Jacobians $J_r^{(i)}$ being computed at the N solutions $\varphi_0^{(i)}$ of eq. (10). The various $J_r^{(i)}$ do not have to be the same, since the functions $\varphi^{(i)}$ are different.

3.3 Boundary of the orbit

The boundary \mathcal{B} of an orbit can be considered as the location of the points leading to the degeneracy of solutions of eq. (10). At a point \mathbf{r}_B of \mathcal{B} , we can say that if φ_B is a solution of $\mathbf{r}(\varphi) = \mathbf{r}_B$, then $\mathbf{r}(\varphi_B + \delta\varphi)$ is also a solution to the second-order in $\|\delta\varphi\|$; we have:

$$\begin{aligned} \mathbf{r}(\varphi_B + \delta\varphi) &\simeq \mathbf{r}(\varphi_B) + \left. \frac{\partial \mathbf{r}}{\partial \varphi} \right|_{\varphi_B} \times \delta\varphi \quad \|\delta\varphi\| \rightarrow 0 \\ &= \mathbf{r}_B + O(\|\delta\varphi\|^2) \end{aligned}$$

if and only if

$$J_r(\varphi_B) \doteq \left| \frac{\partial \mathbf{r}}{\partial \varphi} \right|_{\varphi_B} = 0. \quad (19)$$

We then reach another equivalent definition of the boundary \mathcal{B} , as the location of the points where at least one Jacobian J_r vanishes (and possibly more, since there is a degeneracy of the solutions at this point).

At the boundary, the orbit is divergent in the density (cf. eq. (18)), but this divergence is integrable since the total mass of the orbit is finite.

3.4 Orbital distribution function

The above considerations, related to equations analogous to (8) and (9), directly lead to an expression of the orbital distribution function (DF) $f(\mathbf{r}_0, \mathbf{v}_0)$, by considering

$\left[(2\pi)^2 J_r^{(i)} \right]^{-1}$ as the contribution to the local density ρ from solution i among N :

$$f(\mathbf{r}_0, \mathbf{v}_0) = \frac{1}{(2\pi)^2} \sum_{i=1}^N \frac{1}{J_r^{(i)}} \times \delta(\mathbf{v}_0 - \mathbf{v}(\varphi^{(i)})), \quad (20)$$

where $\varphi^{(i)}, i = 1, \dots, N$ are the solutions to eq. (10). Given the relation (18), this expression is consistent with the basic relation:

$$\rho(\mathbf{r}) \doteq \int f(\mathbf{r}, \mathbf{v}) d\mathbf{v}, \quad (21)$$

where the velocity is an indirect function of the position. Eq. (20) gives the DF at any position \mathbf{r}_0 .

There are several variations for expressing the phase space density, depending whether we are primarily interested in the distribution of the position or of the velocity. For generalization, let us consider a vector κ from a half-subspace (of dimension $n = 2$) of phase-space (of dimension $2n = 4$), and ι from the complementary half-subspace. The previous situation corresponded to $\kappa = \mathbf{r} \equiv (x, y)$ and $\iota = \mathbf{v} \equiv (v_x, v_y)$, but we could have, as we shall see in §3.5, $\kappa \equiv (x_{\text{sky}}, v_{\text{los}})$ and $\iota \equiv (v_{\text{los}}, v_{\text{sky}})$. We now look for an expression of the DF $f(\kappa_0, \iota_0)$ from κ .

In the same way as in the special case $\kappa = \mathbf{r}$ described in §3.2, one can show that:

$$f(\kappa_0, \iota_0) = \frac{1}{(2\pi)^2} \sum_{i=1}^M \frac{1}{J_\kappa^{(i)}} \times \delta(\iota_0 - \iota(\varphi^{(i)})), \quad (22)$$

where this time, we have defined $J_\kappa^{(i)}$ as:

$$J_\kappa^{(i)} \doteq \left| \frac{\partial \kappa}{\partial \varphi} \right|_{\varphi_0^{(i)}}, \quad (23)$$

and with $\varphi_0^{(i)}$ being the multiple solutions of the equation:

$$\kappa(\varphi_0^{(i)}) = \kappa_0, \quad i = 1, \dots, M. \quad (24)$$

The number M of solutions does not have to be the same as the number N of solutions to eq. (10).

3.5 Line-of-sight velocity distribution

Eq. (20) provides the DF $f(\mathbf{r}, \mathbf{v})$ at any point of phase-space accessible to the orbit, and hence allows computation of all the orbital dynamical quantities, directly related to the DF, in particular the line-of-sight velocity distribution (LOSVD).

Once we have chosen a line-of-sight (LOS), associated with coordinates (x', y') (y' along the LOS and x' being in the plane of the sky), we can express the LOSVD $\text{VP}_{x'}(v_{y'})$ (the *velocity profile*) by the usual formula:

$$\text{VP}_{x'}(v_{y'}) \doteq \int_{\text{los}} dy' \int d\mathbf{v}_{x'} f(\mathbf{r}', \mathbf{v}'). \quad (25)$$

We see that, for this purpose, we need an expression for the DF as a function of $\zeta \equiv (x', v_{y'})$. According to eq. (22), we can write:

$$\text{VP}_{x'_0}(v_0) = \frac{1}{(2\pi)^2} \sum_{i=1}^M \frac{1}{J_\zeta^{(i)}}, \quad (26)$$

where the Jacobians $J_\zeta^{(i)}$ are to be computed at the M solutions of the equation:

$$\zeta(\varphi_0^{(i)}) = \zeta_0 \iff \begin{cases} x'(\varphi^{(i)}) &= x'_0, \\ v_y'(\varphi^{(i)}) &= v_0. \end{cases} \quad (27)$$

We can also write down the surface brightness $\mu(x')$ as:

$$\begin{aligned} \mu(x') &\equiv \int_{\text{los}} dy' \int d\mathbf{v}' f(\mathbf{r}', \mathbf{v}') \\ &= \int_{\text{los}} \rho(\mathbf{r}') dy' = \int \text{VP}_{x'}(v) dv, \end{aligned}$$

which gives two equivalent ways to compute these quantities, either from the density, or from the LOSVD.

3.6 Actions

The formalism we use here, based on an expression of the dynamical quantities of the orbit in terms of the angle variables φ , is well-suited for the computation of the actions. An open two-dimensional regular orbit is characterized by exactly two integrals of motion, which can be for instance the two actions \mathcal{J}_1 and \mathcal{J}_2 , that can be defined by (BT87):

$$\mathcal{J}_i \equiv \frac{1}{2\pi} \oint_{\varphi_i \in [0, 2\pi[} \mathbf{v} \cdot d\mathbf{r}, \quad i = 1, 2. \quad (28)$$

Using relations (8) and (9), we obtain after some algebra:

$$\mathcal{J}_{(1)} = \frac{1}{2} \sum_{\lambda} \left[(X_{\lambda}^2 + Y_{\lambda}^2) \binom{l}{m} \lambda \cdot \omega \right]. \quad (29)$$

which is very similar to eq. (16) in Binney & Spergel (1984). As explained by these authors, one is free to define the ‘real’ (useful) actions \mathcal{J}_r and \mathcal{J}_a as any linear combination of the previous quantities, so that it matches any natural requirement such as $\mathcal{J}_r \equiv 0$ for closed long-axis orbits and $\mathcal{J}_a \equiv 0$ for closed loop orbits (BT87). In our case, with the CA98 extraction procedure, we found that the linear transformation to apply was (cf. Fig. 10):

$$\begin{cases} \mathcal{J}_r &= \mathcal{J}_1 & \text{for box orbits,} \\ \mathcal{J}_a &= \mathcal{J}_2 & \end{cases} \quad (30)$$

and

$$\begin{cases} \mathcal{J}_r &= 2\mathcal{J}_2 \\ \mathcal{J}_a &= \mathcal{J}_1 - \mathcal{J}_2 \end{cases} \quad \text{for loop orbits.} \quad (31)$$

This choice guarantees a continuous action space (cf. Binney & Spergel 1984; de Zeeuw 1985).

4 2D NUMERICAL IMPLEMENTATION

We have numerically implemented the formalism described above, and in §4.1 describe tests on orbits in a two-dimensional separable potential for which all relevant quantities are known analytically. We then consider a non-integrable logarithmic potential in §4.2.

4.1 Sridhar & Touma potential

We first study an orbit in a two-dimensional separable potential, described by Sridhar & Touma (1997; see Appendix A). This potential is of Stäckel form in parabolic coordinates, and allows a complete analytic study of the

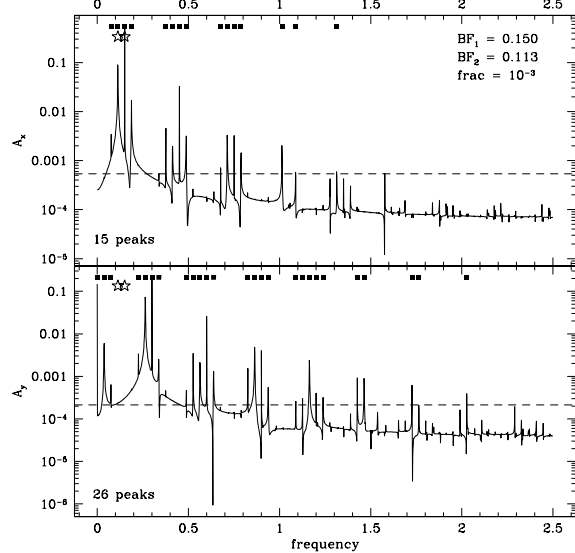


Figure 2. Fourier spectra (amplitude vs. frequency) for the test orbit. The selected frequencies for the decomposition (squares) are those of amplitude A_i larger than $F \max[A_i]$ in each coordinate, indicated by the long-dashed lines, with $F = 10^{-3}$ (giving 15 peaks in x and 26 in y). The two base frequencies are marked by stars.

orbits (in particular computation of the boundaries and expression of the surface density), which are all regular, and usually denoted as banana orbits.

The illustrations in this section are made for a slightly cusped potential ($\alpha = 0.5$, with notations of Appendix A), and a test-orbit with energy $E = 2.39$ and second integral $I_2 = 0.38$, integrated on 4096 points over 123 periods with a 7/8th order Runge-Kutta integrator (Fig. 3).

4.1.1 Spectral analysis and time-dependent expressions

The Fourier spectra $\hat{x}(\nu)$ and $\hat{y}(\nu)$ of the time series of the coordinates $x(t)$ and $y(t)$ of a quasiperiodic orbit, obtained in the usual way by numerical integration, consist of discrete lines whose frequencies are linear combinations of the base frequencies. We modified an algorithm provided by CA98 for the extraction of the base frequencies, in order to give all the quantities defining the Fourier series (4). The CA98 method computes the Fourier transform of the coordinates of an integrated orbit, identifies the peaks in the Fourier spectra and extracts the corresponding frequencies. It looks for the base frequencies, and linearly decomposes the selected frequencies over these BFs (see Fig. 2). The output then consists of: the base frequencies ω , and for each peak frequency in each coordinate, the linear decomposition over the base frequencies (e.g., $\lambda \equiv (l, m)$), and the associated amplitude (X_{λ}) and phase (χ_{λ}).

The CA98 algorithm provides a finite number of terms in the quasi-periodic expansion (4). The selection is made by keeping, in each coordinate, only frequencies with amplitude greater than a fraction F of the greatest one (typically $F = 10^{-2}$ – 10^{-3} , depending on the required accuracy), giving a finite number of terms in each direction (typically between 10 and 20). The numerical approximations obtained

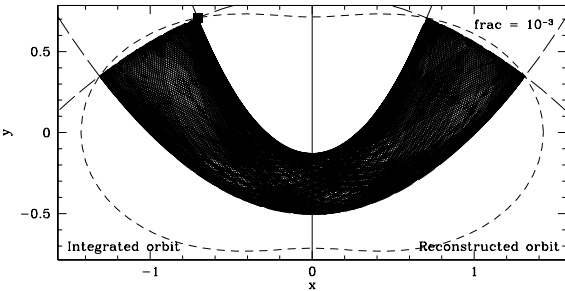


Figure 3. Comparison between time expression from numerical integration (left) and spectral expansion (right) of an orbit in the Shridhar & Touma potential. The spectral time-dependent expansion (4) was obtained with $F = 10^{-3}$ (resulting in 15 frequencies in x and 26 in y) at the same time-steps as the integrated orbit. The short-dashed line is the Zero-Velocity Curve (zvc), and the long-dashed curves indicate the boundaries of the orbit calculated by using the separable nature of the potential (cf. Appendix A). The orbit was launched from the zvc (square). The boundaries of the reconstructed orbit are barely distinguishable from the exact boundaries, indicating the level of precision of the expansion.

by the truncation of the series coincide with the actual expansion (4) up to the required accuracy (Fig. 3).

4.1.2 φ -expressions

The time-dependent expansion (4) provides a semi-analytic expression for a regular orbit. It can be useful for storage purposes, or for extrapolating orbital motion to times much longer than the actual integration time (e.g., in order to reduce the numerical noise of a grid-based density computation). However, time is not a good variable for a regular orbit that will eventually fill up completely its invariant torus, and the angle variables φ should be used instead. This leads to the expressions (8) and (9) for $x(\varphi)$ and $y(\varphi)$, respectively.

The problem is then to recover the N different solutions of eq. (10) for a given position \mathbf{r}_0 . First, we have to find the expected number N of solutions. This is inferred from the orbit classification, according to the criteria described in §3.1. We then use standard root-finding routines (in our case, the NAG routine C05PBF) from different initial conditions until we have found the N solutions, or until a maximum number of trials, indicating a degenerate case with fewer solutions (see Fig. 4). Interestingly, there is point-symmetry in the solutions. For example, for the Sridhar & Touma banana orbit in Fig. 4, the center of the symmetry is at $\varphi = (\pi, \pi)$. In fact this is true for *any* box orbit in a general non-rotating potential as well. This is because we can always choose the corner of a box orbit as the initial conditions, i.e., $\mathbf{v} = \varphi = \mathbf{0}$ at $t = 0$. Then for any box described by $\mathbf{r}(t)$, we can generate the new orbit described by $\mathbf{r}(-t)$ by reversing the arrow of the time, and the new orbit simply *repeats* the old one with $\mathbf{r}(-t) = \mathbf{r}(t)$: reversing has no effect on the orbit because the initial velocity is zero. This time-symmetry means $\varphi[2\pi]$ and $-\varphi[2\pi]$ describe the same point in the configuration space, where the modulus brings the phase angle to the default interval $[0, 2\pi]$. Thus the solutions come in pairs at φ and $2\pi - \varphi$ with point-symmetry around (π, π) . The

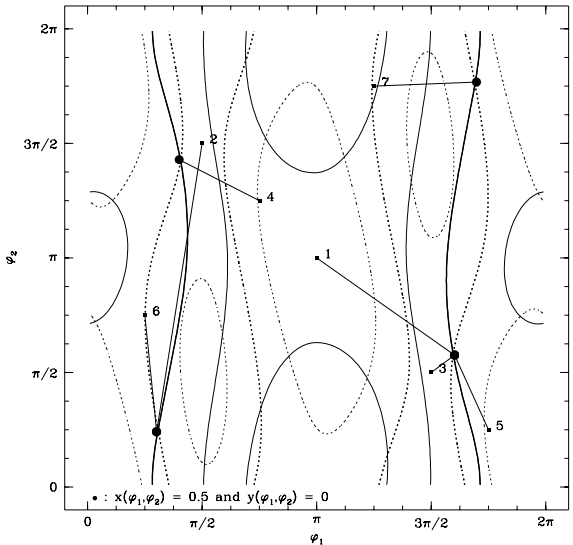


Figure 4. Contours of $x(\varphi)$ (solid lines) and $y(\varphi)$ (dotted lines), for the test orbit reconstructed with $F = 10^{-3}$. The levels $x = x_0 = 0.5$ and $y = y_0 = 0$ (thick lines) intersect at the $N = 4$ values of $\varphi(\mathbf{r}_0)$ (dots). Successive initial conditions for the root-finding routine (squares) lead to different solutions (straight lines), until it finds the expected number of solutions.

above arguments do not apply to loop orbits because there is no point in a loop where the velocity is zero[†].

4.1.3 Density maps and velocity profiles

Eq. (18) allows the computation of the orbital density at any point \mathbf{r}_0 once we have determined the N solutions of eq. (10) by the appropriate root-finding routine. Since the test orbit was integrated in a Stäckel potential, the derived density distribution can be compared to the analytic expression available for this case (cf. Appendix A). Fig. 5 shows contours of the two densities side by side with the same levels. The spectral density was obtained from an expansion truncated in amplitude with $F = 10^{-3}$, giving 15 terms in x and 26 in y . The indicated masses, which should be unity by construction in both cases, are computed from a numerical integration over the density grid; it can be therefore used as a rough estimate of the precision of the density computation.

As expected, the more terms are kept in the series (4), the more accurate the representation of the orbit (Fig. 5). With $F = 10^{-2}$, the orbit is represented by an expansion with 4 terms in x and 12 terms in y , and the density is recovered to $\sim 20\%$. When F is set to 10^{-3} (Fig. 5), the expansion contains 15 terms in x and 26 in y , and the density is accurate to $\sim 3\%$ in the inner parts of the orbit, and degrades very close to the boundaries of the orbit due to the divergence of the density there. This precision in density can be compared with the usual computation of the density, directly during integration (see §4.3).

[†] Reversing the arrow of time from a initial point at say, $x = 0, y = 1$ of a loop, will lead to a counter-loop with identical shape indeed, but for which φ and $2\pi - \varphi$ correspond to two different points in configuration space, with $(x(-t), y(-t)) = (-x(t), y(t))$.

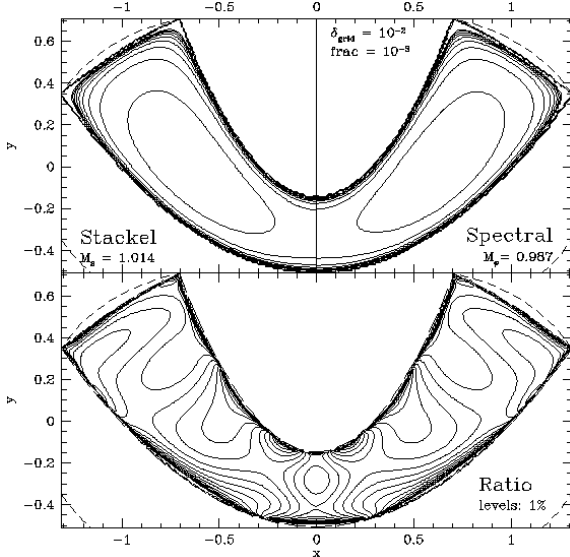


Figure 5. *Upper panel:* Orbital density distribution in the Shridhar & Touma potential computed from spectral theory (*right*) compared with the exact expression (*left*). The spectral density (18) was obtained with $F = 10^{-3}$ on the same grid as the Stäckel density (step $\delta_{\text{grid}} = 10^{-2}$). The density levels range from 0 to 2 in 11 steps. The total mass of the orbit is normalized to 1 by definition in each case. *Lower panel:* Ratio between spectral density and Stäckel density, in the case $\text{frac} = 10^{-3}$. The contour levels range linearly from 0.9 to 1.1 in steps of 0.01 (thick line $\equiv 1$). The increased discrepancy close to the boundary of the orbit is due to the divergence of the density and its associated numerical imprecision.

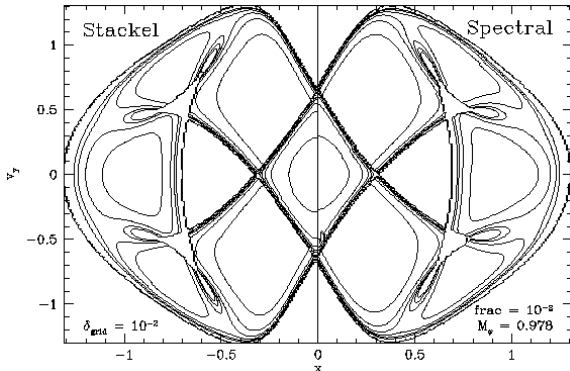


Figure 6. Position-velocity diagram (PVD), i.e., density in the plane (x, \dot{y}) , for the test-orbit, computed from Stäckel expression (*left*) and from spectral theory with $F = 10^{-3}$ (*right*). The contours range linearly from 0 to 0.4 in 9 steps. Since the orbit is a banana orbit, hence a boxlet orbit without a definite sense of rotation, the PVD is symmetric with respect to $\dot{y} = 0$.

Using eq. (26), we can also compute the velocity profile along any line-of-sight, and gather in a position-velocity diagram (PVD) all the velocity profiles corresponding to parallel LOS. This is the projected density of the phase-space orbit on the plane (x', v_y) (where x' and y' are the coordinates running perpendicular and parallel to the LOS), in the same way as the ‘density’ corresponds to the projected density of the phase-space orbit on the plane (x, y) . A cut of this PVD

along a given x'_0 would give the LOSVD along a line-of-sight running parallel to the y' -axis and going through x'_0 . Fig. 6 presents side by side the PVD of the test-orbit for a LOS parallel to the y -axis, computed from the Stäckel formalism (*left*) and from the spectral theory (*right*), using the same spectral expansion as before. Precision of the computation is as expected ($\sim 10\%$, see §4.2.1).

4.2 Logarithmic potential

We now consider a non-integrable potential of astronomical interest, the logarithmic potential (BT87, p.126):

$$\Phi(x, y) \doteq \frac{1}{2} v_0^2 \ln \left(R_c^2 + x^2 + \frac{y^2}{q^2} \right), \quad (32)$$

with v_0 the circular speed at large radius, R_c the core radius, and q the axial ratio of the equipotentials. Positivity of the associated density requires $1/\sqrt{2} \leq q \leq 1$. This potential admits two major families of orbits (BT87), the box orbits and the flat-tube or loop orbits, accessible from different initial conditions. For the illustrations, we consider the case $v_0 \equiv R_c = 1$ and $q = 0.9$.

4.2.1 Density maps and velocity profiles

Two orbits of the same energy $E = 1.629$ were integrated: a box orbit over 128 periods, and a loop orbit over 167 periods (cf. Fig. 7). This energy gives a ZVC such that $x_{\text{ZVC}}/R_c = 5$, where x_{ZVC} corresponds to the intersection of the ZVC with the x -axis.

From eq. (18), we then compute the density map of each orbit from a spectral analysis set by $F = 10^{-3}$, giving position expansions with 11 terms in x and 17 in y for the box orbit, and 13 terms in x and 12 in y for the loop orbit (right panels of Fig. 7).

Fig. 8 presents the PVD of the two previous orbits for a LOS parallel to the y -axis. The ‘wiggles’ that can be seen in the middle of the loop orbit PVD (Fig. 8 lower panel) are a numerical artifact, at the $\sim 10\%$ level. The origin of this can easily be understood: for an orbit in logarithmic potential (32), the characteristic length scale, velocity and frequency are of the order x_{ZVC} , v_0 and $|\omega| \sim v_0/x_{\text{ZVC}}$. When we truncate the expansion (8) of the coordinate $x(\varphi)$ according to the parameter F , we make a relative error at the level $X_\lambda/x_{\text{ZVC}} < F$ with the coordinate, where X_λ is the amplitude of the truncated term. Meanwhile, the corresponding term in the velocity expansion (9) has an amplitude $\lambda \cdot \omega X_\lambda$, where the frequency of the expansion term $\lambda \cdot \omega$ increases linearly as we go to higher and higher order terms. So the corresponding error with the velocity is at the level $\lambda \cdot \omega X_\lambda/v_0 \sim |\lambda| X_\lambda/x_{\text{ZVC}} < |\lambda| F$. So while the same truncation reproduces the orbital position and position-related quantities such as the density within a few percents, it may significantly over- or under-estimate the high frequency variations in the orbital velocity and for velocity-related quantities such as LOSVD’s. A way to correct for this effect would be to truncate the different expansions according to the higher amplitude X_λ or $\lambda \cdot \omega X_\lambda$ at a given order (Papaphilippou & Laskar 1996). While truncating according to the amplitudes X_λ is straightforward, truncating according to $\lambda \cdot \omega X_\lambda$ requires a priori knowledge of the BF decomposition (λ, ω) ,

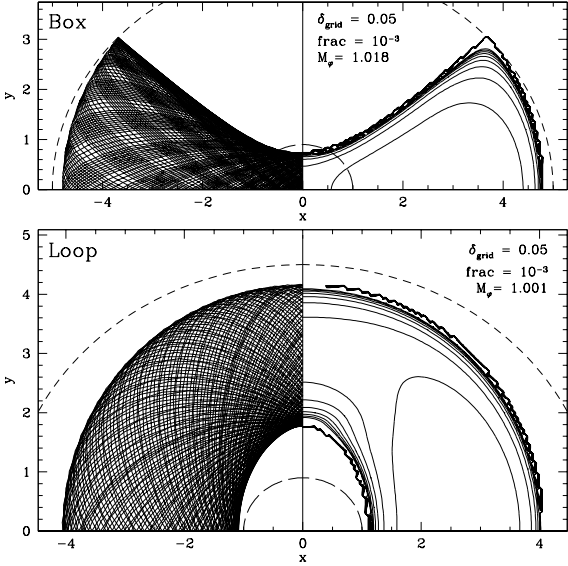


Figure 7. *Upper panel:* Integrated box orbit (left) and spectral density (right) computed from an expansion truncated at $F = 10^{-3}$ on a grid of step $\delta_{\text{grid}} = 10^{-2}$. The contours range from 0 to 0.1 in 11 steps. The short-dashed line is the zvc, and the long-dashed line corresponds to the core of the potential. *Lower panel:* Same as previous, but for the $y > 0$ -side of the loop orbit. The contours range from 0 to 5.10^{-2} in 11 steps.

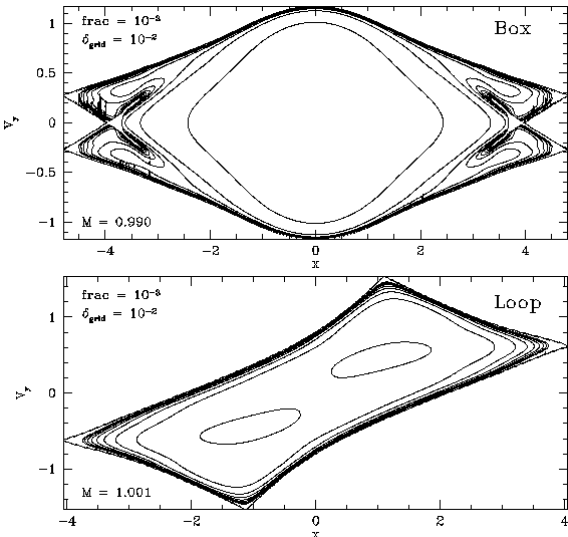


Figure 8. *Upper panel:* PVD for the box orbit, with contours ranging linearly from 0 to 0.3 in 11 steps. Notice the symmetry of the PVD with respect to $\dot{y} = 0$. *Lower panel:* Same as previous, but for the loop orbit. The contours range linearly from 0 to 0.2 in 11 steps. Since the loop orbit has a definite sense of rotation (here, anti-clockwise), the PVD only has reflection symmetry with respect to the point $(x, \dot{y}) = (0, 0)$.

which generally would mean a double pass, and hence a significantly increased number of computations. We have not followed this route here, as this additional accuracy will play only a minor role in most practical applications, such as the computation of the moments of the LOSVD.

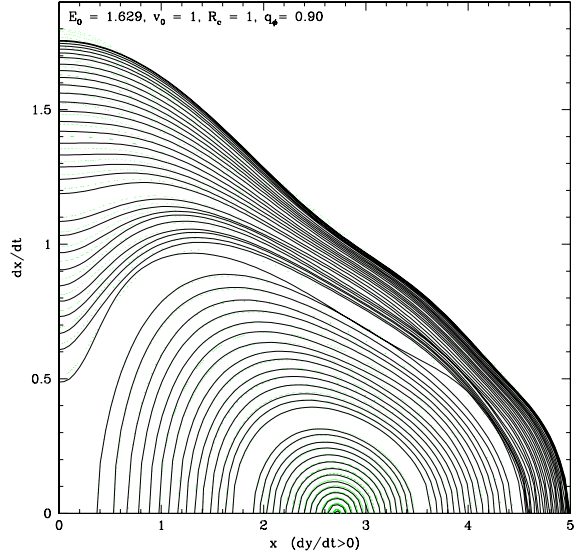


Figure 9. Surface of section (x, \dot{x}) , $\dot{y} \geq 0$ computed from 60 regular open orbits of energy $E = 1.629$, for a truncation fixed by $F = 10^{-3}$. Only the low-resonance orbits which do not overlap over themselves, have been kept. The empty areas correspond either to stochastic areas or ‘high’-resonance islands. Dots correspond to the construction of the surface of section of each orbit during its short numerical integration (see text).

4.2.2 Surface of section and action space

We have integrated a complete library of orbits in the logarithmic potential (32). All the orbits have the same energy $E = 1.629$, and are integrated over typically ~ 150 periods with 4096 time-steps. The 140 initial conditions (ICs) are distributed according to: 40 ICs evenly spaced in angle on the zvc, and thus with zero initial velocity so that they are boxes or irregular orbits, and 100 ICs evenly spaced in radius along the short axis ($x = 0$ and $y > 0$), with an initial velocity vector perpendicular to the axis ($v_x > 0$ and $v_y = 0$). Those with $y < y_b$, where y_b is the amplitude of the last stable y -axis oscillation, are boxes or irregular orbits. The remainder are loops. With the exception of the closed loop at the chosen energy, these all cross the y -axis perpendicularly in two points. We keep only those that cross at apocenter, and furthermore remove all high-order resonant orbits, leaving a total of 60 regular, open, ‘low-resonance’ boxes and loops. The spectral analysis of each integrated orbit is carried out with $F = 10^{-3}$, giving typically ~ 13 terms in the expansions along x and y .

We constructed the surface of section (x, \dot{x}) , $\dot{y} \geq 0$ for this library by solving for the velocity (\dot{x}, \dot{y}) at each point $(x, y = 0)$ of an orbit. The result is shown in Fig. 9. Since we kept only low-resonance orbits, this surface of section does not show any resonant island. However, the discarded orbits leave empty areas in the surface of section between the regular loops and boxes. For comparison, we also show in Fig. 9 the surface of section from the short orbital integration (~ 150 periods). As already noted in §4.2.1, the velocity is less accurately retrieved in the spectral process than the position, which results in some small differences (few percents) in the surface of section.

Using expression (29), we computed the actions as

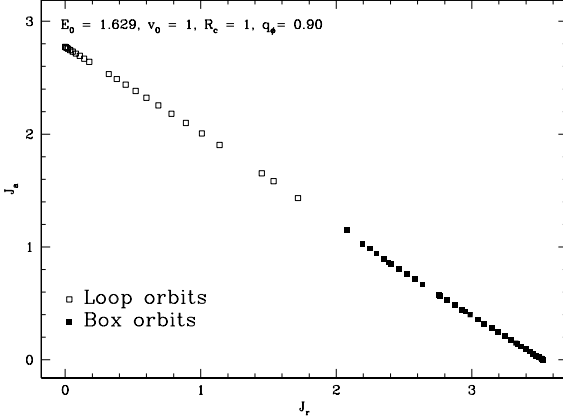


Figure 10. Action space J_a , vs. J_r computed from the same orbital set as Fig. 9 and with the same truncation of the expansion. Note the natural distinction occurring between box orbits (solid squares) and the loop orbits (open squares). The two straight sequences meet in the middle as in Fig. 3-25 of BT87. The gaps in the surface of section plot are seen here as well.

sociated with an orbit, and constructed the action-space (J_r, J_a) of the mono-energetic library (Fig. 10). This visualization of the library in action-space is of particular interest: since the action-angle variables are canonical, and their integration is particularly simple (§2.1), equal volume in action space is directly associated to equal volume in phase-space (Binney & Spergel 1984). This provides a two-dimensional representation of the four-dimensional phase-space. As expected, a natural dichotomy between box orbits (solid squares) and loop orbits (open squares) appears in this space.

4.3 Numerical discussion

The traditional way of computing the orbital density, just as any other dynamical quantity such as the LOSVD, is the following: along the orbital motion (during the numerical integration), and for a predetermined grid in configuration space, one counts up the number of integration points falling in a given cell (e.g., Rix et al. 1997). This gives the total fraction of time spent in this cell, which is proportional to the local density after a long enough integration time.

For a sufficiently fine grid, this process of ‘dropping balls in buckets’ can be considered as a random process, and the statistical noise associated with a count of N points in a cell is $\sim \sqrt{N}$, leading to a precision in density of order $1/\sqrt{N}$. The orbit in Fig. 5 was integrated for 4096 points, and the density represented on a grid with step $\delta_{\text{grid}} = 10^{-2}$. Assuming that the integration points are approximately uniformly distributed over the whole area accessed by the orbit, roughly $2 \times 0.5 = 1$ or $1/\delta_{\text{grid}}^2 = 10^4$ cells, the average number of points per cell is ~ 0.5 , leading to a very low precision in density ($> 100\%$). A precision of the same order of the one obtained with spectral dynamics ($\lesssim 5\%$), would require integrating ~ 800 times longer, in order to get ~ 400 points per cell.

Fig. 11 and 12 compare in a more quantitative way the spectral density (dotted line) and the ‘bucket’ densities (solid line) computed for different integration times for the box and

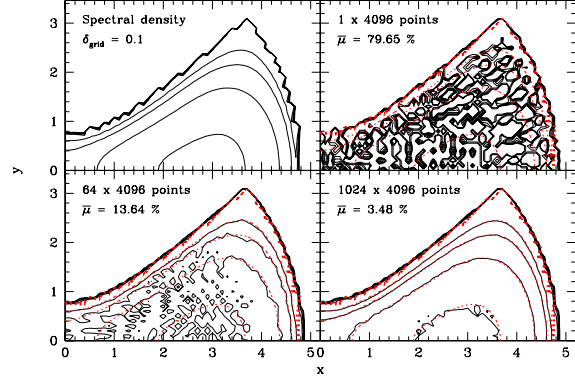


Figure 11. Comparison, for the $x > 0$, $y > 0$ part of the box orbit of Fig. 7, between the spectral density (upper left panel and dotted line in other panels) and the ‘bucket’ densities (solid line in other panels) for different integration times, related to the number of points. In both cases, contour levels range logarithmically from $1.35 \cdot 10^{-4}$ to $4 \cdot 10^{-4}$ in 4 steps, and the step of the grid used for the computation of the density is $\delta_{\text{grid}} = 0.1$. The mean accuracy $\bar{\mu}$ is defined in the text.

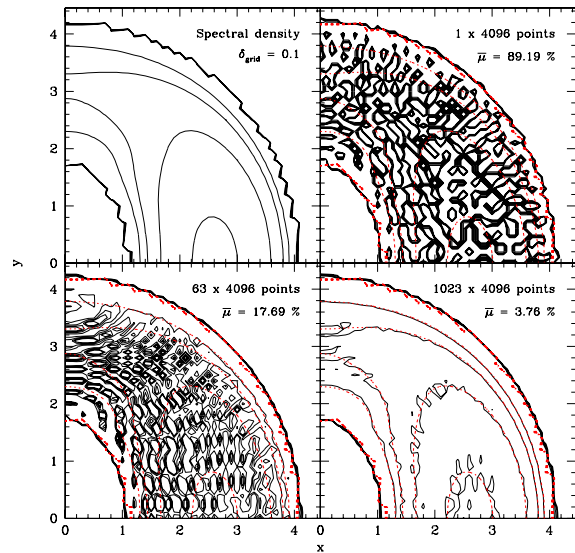


Figure 12. Same as Fig. 11, but for loop orbit of Fig. 7. Contour levels range logarithmically from $1.1 \cdot 10^{-4}$ to $2.3 \cdot 10^{-4}$ in 4 steps.

loop orbits shown in Fig. 7. The estimated mean accuracy $\bar{\mu}$ is defined as $\bar{\mu} \equiv \langle 1/\sqrt{N_i} \rangle$, where N_i is the number of balls in bucket i , and $\langle \cdot \rangle$ is the average over all the non-empty cells. As expected, the mean accuracy is directly related to the number of integration points used during the computation of the density. It can be clearly seen in both cases that 4096 points along the orbit, typically needed for the torus reconstruction from spectral analysis, are *highly* insufficient for computing a proper ‘bucket’ density.

Fig. 13 compares the different mean accuracies obtained in terms of computing power. The CPU-time is expressed in arbitrary units. Each density was computed on the same computer, and the time used by each process was renormalized to the shortest one (a few seconds on a standard Linux station). The spectral mean accuracy is estimated to be $\sim 3\%$ (cf. §4.1.3). We conclude that the spectral density

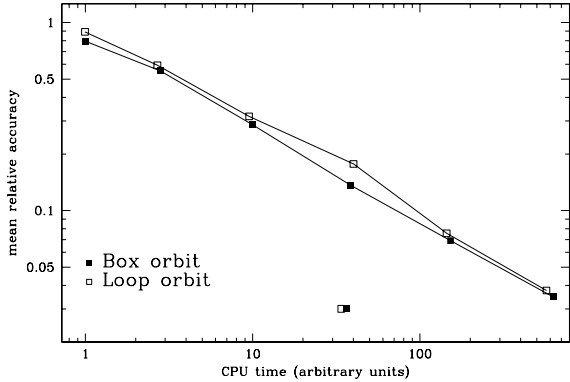


Figure 13. Mean accuracy of the density computations *vs.* computing power needed for the computation, for the previous box (solid symbols) and loop (open symbols) orbits. Each dot on the lines corresponds to a case in Fig. 11 or 12, while the isolated symbols give an estimate of the spectral density mean accuracy ($\sim 3\%$).

is almost one order of magnitude more accurate than the ‘bucket’ density for the same computing power.

5 AXISYMMETRIC POTENTIALS

Recent work on modeling the internal dynamics of elliptical galaxies, aimed at measuring masses of central black holes or the distribution of extended dark matter, compare stellar absorption line kinematics with fully general three-integral multi-component axisymmetric models. While in some cases semi-analytic approaches can be used (e.g., Matthias & Gerhard 1999), many studies use a variant of Schwarzschild’s orbit superposition technique (e.g., van der Marel et al. 1998; Cretton & van den Bosch 1999; Gebhardt et al. 1999; Cretton, Rix & de Zeeuw 1999). In this approach, orbits are calculated numerically in a chosen potential, and their properties are projected onto the plane of the sky. These are then combined to reproduce the observed surface density and LOSVD’s. The current implementations use the ‘bucket’ method for calculating the orbital properties.

Motion in a three-dimensional axisymmetric potential can be reduced to a two-dimensional problem by exploiting the conservation of the z -component of the angular momentum L_z (e.g., BT87), and describing the motion in the meridional plane (R, z) (the angular variable ϕ being cyclic). The properties of a regular orbit in such a potential can thus be computed with much improved accuracy by means of a minor adaptation of the spectral dynamics formalism described in the above, and we present the relevant equations here, together with some examples.

The illustrations are made for a test-orbit with energy $E_0 = -0.8$ and angular momentum $L_z = 0.2$ integrated in the meridional plane of a three-dimensional axisymmetric coreless logarithmic potential:

$$\Phi(R, z) \hat{=} \frac{1}{2} v_0^2 \ln \left(R^2 + \frac{z^2}{q^2} \right), \quad (33)$$

with $q = 0.9$ and $v_0 = 1$. Hereafter, we use $\alpha \hat{=} i - \pi/2$, where i is the usual inclination angle of a galaxy ($i = 0$ for a face-on galaxy).

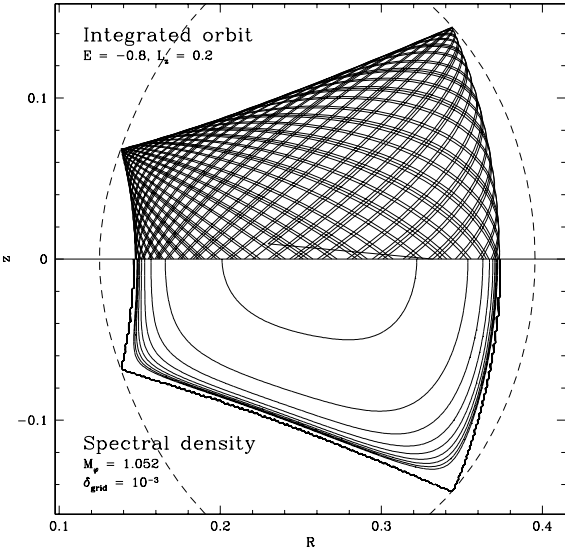


Figure 14. Three-dimensional axisymmetric orbit integrated in the meridional plane (*upper part*) and its associated meridional density computed from spectral analysis (*lower part*).

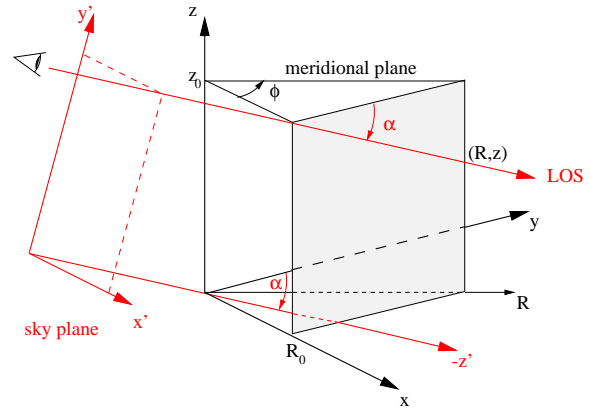


Figure 15. Notations used in the text for the conversion of two-dimensional to three-dimensional densities. We use $\alpha = i - \pi/2$, where i is the customary inclination of the galaxy (> 0 when seen from above).

5.1 Spatial density

If the density of an orbit in the meridional plane is $\rho_M(R, z)$, the associated spatial density is simply

$$\rho(R, z, \phi) = \frac{\rho_M(R, z)}{2\pi R}, \quad (34)$$

where the factor 2π ensures the normalization, so that $\int \rho M dR dz = \int \rho dR dz d\phi = 1$.

Fig. 14 shows an example of the density of an orbit in the meridional plane, reconstructed with the spectral formalism.

5.2 Projected intensity

Cartesian coordinates (x', y') on the plane of the sky relate to spatial cylindrical coordinates (R, ϕ, z) as follows (see Fig. 15):

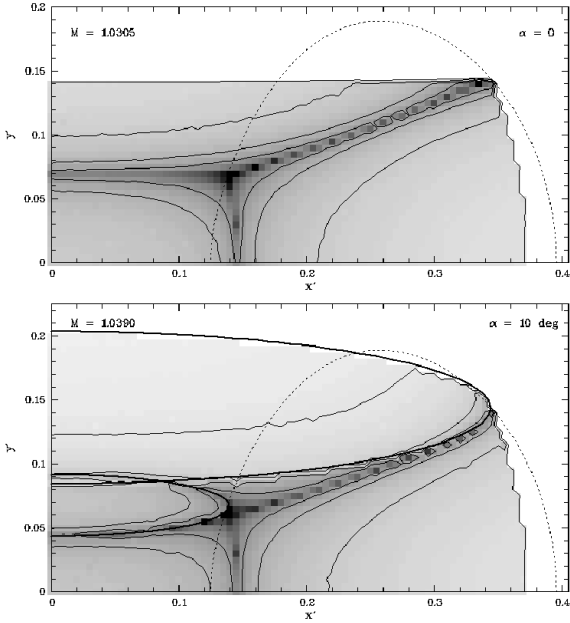


Figure 16. Sky density computed for the test-orbit seen edge-on ($\alpha = 0$, upper panel) and slightly overhead ($\alpha = 10^\circ$, lower panel). Dotted line: ZVC in the meridional plane. Note how the divergence of the density at the boundaries of the orbit in the meridional plane translates in sky density. Heavy line: geometrical location of the ‘corners’ of the orbit. The numerical line-of-sight integration precision is set to 10^{-2} .

$$\begin{cases} x' = R \cos \phi, \\ y' = z \cos \alpha - R \sin \phi \sin \alpha, \end{cases} \quad (35)$$

where α defines the orientation of the line of sight. Assuming $\alpha \neq \pm\pi/2$ (i.e., the galaxy is not seen face-on), we find

$$\begin{cases} R_{x',y'}(\phi) = |x'| / \cos \phi, \\ z_{x',y'}(\phi) = y' / \cos \alpha + |x'| \tan \alpha \tan \phi. \end{cases} \quad (36)$$

Furthermore, since $dz' = -dy / \cos \alpha$ and $dy = R d\phi / \cos \phi$,

$$dz' = \frac{|x'| d\phi}{\cos \alpha \cos^2 \phi}. \quad (37)$$

We can then compute the intensity on the sky $I_\alpha(x', y') \doteq \int_{\text{los}} \rho(R, z, \phi) dz'$ for $x' \neq 0$, to obtain:

$$I_\alpha(x', y') = \frac{1}{2\pi} \int_{-\pi/2}^{\pi/2} \frac{\rho_M(R_{x',y'}(\phi), z_{x',y'}(\phi)) d\phi}{\cos \alpha \cos \phi}. \quad (38)$$

The integrand is not singular at the limits of integration, since an orbit reaches a maximum radius R_{\max} in the meridional plane, corresponding to a maximum angle $\phi_{\max} \doteq \arccos(R_0/R_{\max})$ (for $R_0 \leq R_{\max}$; otherwise, we know that $I \equiv 0$). Equivalently, the orbit reaches a minimum radius R_{\min} , corresponding to the angle $\phi_{\min} \doteq \arccos(R_0/R_{\min})$ (or 0 if $R_0 > R_{\min}$). We can therefore restrict the integration domain to the segments $[-\phi_{\max}, -\phi_{\min}] \cup [\phi_{\min}, \phi_{\max}]$.

Similarly, for $x' = 0$, we obtain

$$I_\alpha(x' = 0, y') = \int_{R_{\min} / \cos \alpha}^{R_{\max} / \cos \alpha} \sum_{\pm} \rho_{y'}^{\pm}(z') \frac{dz'}{z' \cos \alpha}. \quad (39)$$

where we have defined $\rho_{y'}^{\pm}(z') \doteq \rho_M(z' \cos \alpha, \frac{y'}{\cos \alpha} \pm z' \sin \alpha)$.

Fig. 16 shows the upper-right quadrant of the projected density on the plane of the sky of the test orbit when seen

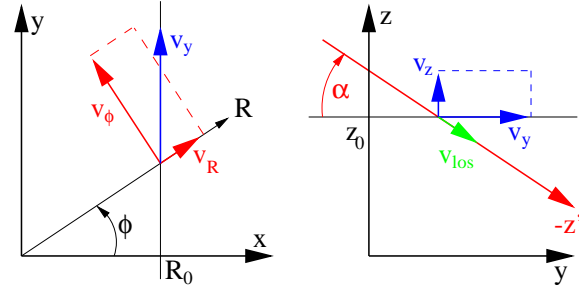


Figure 17. Elements of geometry for the computation of the velocity along the LOS.

edge-on ($\alpha = 0$) or slightly overhead ($\alpha = 10^\circ$). As the computation of the projected intensity involves an extra numerical integration, the result is more sensitive to numerical errors in the determination of the orbital density in the meridional plane. Fig. 16 has been obtained with an integration relative precision set to 10^{-2} .

5.3 Line-of-sight velocity distribution

The velocity v_{los} along the LOS (cf. Fig. 17) is given by

$$v_{\text{los}} = \left(\frac{L_z}{R} \cos \phi + v_R \sin \phi \right) \cos \alpha + v_z \sin \alpha, \quad (40)$$

where v_R and v_z are the velocity components in the meridional plane, and $v_\phi = L_z/R$. The LOSVD can then be computed as follows:

$$\text{VP}_{x',y'}(v_{\text{los}}) = \frac{1}{(2\pi)^3} \sum_{i=1}^M \frac{1}{J^{(i)}}, \quad (41)$$

where the Jacobian

$$J^{(i)} \doteq \frac{\partial(x', y', v_{\text{los}})}{\partial(\phi_1^{(i)}, \phi_2^{(i)}, \phi_3^{(i)})}, \quad (42)$$

is to be evaluated at the i -th solution $\varphi^{(i)} \equiv (\phi_1^{(i)}, \phi_2^{(i)})$, $i = 1, \dots, M$, of the system of equations:

$$\begin{cases} y' = z(\varphi^{(i)}) \cos \alpha - R(\varphi^{(i)}) \sin \alpha \sin \alpha, \\ v_{\text{los}} = \left(\frac{L_z}{R(\varphi^{(i)})} \cos \phi + v_R(\varphi^{(i)}) \sin \phi \right) \cos \alpha \\ \quad + v_z(\varphi^{(i)}) \sin \alpha. \end{cases} \quad (43)$$

The reason that we need only to solve for two action angles $\phi_1^{(i)}$ and $\phi_2^{(i)}$ for the motion in the meridional plane is that the third angle $\phi_3^{(i)}$ is simply the azimuthal angle ϕ , which is related to the two action angles $\varphi^{(i)}$ by

$$\phi_3^{(i)} \equiv \phi = \arccos \left[\frac{x'}{R(\varphi^{(i)})} \right]. \quad (44)$$

Fig. 18 shows the position-velocity diagram of the test-orbit as seen with a ‘virtual’ long-slit placed along the x' -axis (that is $y' = 0$). By symmetry, we can restrain the study to the part $x' \geq 0$, where the velocities are expected to be mostly positive since $L_z > 0$.

6 CONCLUSIONS

We have used the spectral analysis code provided by Carpintero & Aguilar (1997) to determine the properties of orbits

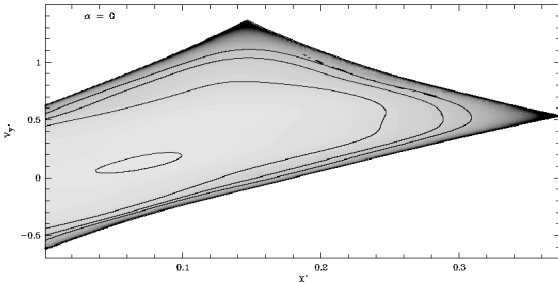


Figure 18. PVD for a ‘virtual’ long-slit placed along the x' -axis ($y' = 0$) of the test-orbit seen edge-on ($\alpha = 0$). The intensity at a point $(x', y' = 0, v_{\text{los}})$ is computed by means of eq. 41.

in elliptic disks and in axisymmetric potentials based on numerical integration over a modest number of orbital periods. We have approximated regular orbits by a truncated Fourier time series of a few tens of terms per coordinate, and have reconstructed the underlying invariant torus by computation of the associated action-angle variables. We have used this to relate the uniform distribution of a regular orbit on its torus to the non-uniform distribution in the familiar space of observables by a simple Jacobian transformation between the two sets of coordinates. This approach is by no means new, but we have extended the published formalism to include calculation of the quantities used in the construction of dynamical models by Schwarzschild’s method, in particular the orbital density and the observed LOSVD’s for elliptic disks and for axisymmetric models.

In the standard implementation of Schwarzschild’s method, orbital properties are recorded on a grid of cells in configuration space (x, y, z) and in the space of observables (x', y', v_{los}) (e.g., Cretton et al. 1999). The number of cells is generally taken to be of the order of 1000-2000, and orbital densities and kinematic properties are calculated by numerically integrating an orbit for a very long time, so that each cell is crossed at least 100 times. Averaging of the time spent in the cell, or of the velocity distribution in the cell, then results in a $\sim 10\%$ accuracy on the orbital density and the observed kinematics. By contrast, the spectral method allows the invariant orbital torus to be described by a few tens of terms, and allows computation of all the physical quantities in a cell-independent way with much increased accuracy. At a given accuracy, the spectral method requires less cpu time than the traditional approach, at least for the two-dimensional cases we have investigated. The resulting flexibility in the determination of the orbital properties, and the drastic reduction of storage space for the orbit library, provide further significant improvements in the practical application of Schwarzschild’s method.

The algorithm devised by CA98 uses only the orbital position for spectral analysis. It truncates the orbital Fourier series according to a criterion on the spectra of the coordinates, so that the resulting Fourier series approximation and torus reconstruction is less accurate in velocity space. Laskar’s (1993) NAFF algorithm uses the complete phase-space position, and may therefore be more efficient in the determination of the base frequency of an orbit and in the torus reconstruction. However, the precision obtained with CA98 seems adequate for the practical goals of the method.

The method employed here to compute orbital prop-

erties works best for the main families of regular orbits. The higher-order resonances (e.g., Miralda-Escudé & Schwarzschild 1989) can be found by the CA98 algorithm, but the torus reconstruction becomes more difficult (e.g., Kaasalainen 1995). This suggests that the main advantage will lie in the construction of dynamical models that have a fairly regular phase space, such as models with central density profiles that are only moderately cusped.

Irregular orbits cannot be represented by our Fourier series expansions. In principle it is possible to obtain the properties of these orbits by subtracting the contributions of the regular ones from an $f(E)$ or $f(E, L_z)$ component (e.g., Zhao 1996; Cretton et al. 1999), which can be represented as the sum of all regular and irregular orbits at that E (and L_z). Use of the smooth regular orbits and the $f(E)$ and $f(E, L_z)$ components as building blocks in Schwarzschild’s method therefore means that the irregular orbits are included as well.

Application of spectral dynamics to compute the observable properties of regular orbits in genuinely three-dimensional potentials is possible in principle. Construction of triaxial dynamical models that fit observed the kinematics of early-type galaxies may well benefit from the same approach, although the rich phase space, and the presence of many irregular orbits, may complicate its practical application (e.g., Häfner et al. 1999).

It is a pleasure to thank Luis Aguilar and Daniel Carpintero for making available their spectral dynamics code, and to thank Wyn Evans for constructive comments.

REFERENCES

Arnold V.I., 1989, Mathematical Methods of Classical Mechanics, Springer-Verlag, New-York
 Binney J., Kumar S., 1993, MNRAS, 261, 584
 Binney J., Spergel D., 1982, ApJ, 252, 308
 Binney J., Spergel D., 1984, MNRAS, 206, 159
 Binney J., Tremaine S., 1987, Galactic Dynamics, Princeton University Press, Princeton (BT87)
 Carpintero D. D., Aguilar L. A., 1998, MNRAS, 298, 1 (CA98)
 Cretton N., de Zeeuw P. T., van der Marel R. P., Rix H. W., 1999, ApJS, 124, 383
 Cretton N., Rix H.-W., de Zeeuw P.T., 2000, ApJ, in press
 Cretton N., van den Bosch F. C., 1999, ApJ, 514, 704
 de Zeeuw P. T., 1985, MNRAS, 216, 273
 Gebhardt K., Richstone D., Kormendy J., Lauer T., Ajhar E., Bender R., Dressler A., Faber S., Grillmair C., Magorrian J., Tremaine S., 2000, AJ, in press
 Goldstein H., 1980, Classical Mechanics, 2nd edn. Addison-Wesley, Reading Mass.
 Häfner R., Evans N.W., Dehnen W., Binney J., 1999, MNRAS, in press astro-ph/9905086
 Kaasalainen M., 1994, MNRAS, 268, 1041
 Kaasalainen M., 1995, MNRAS, 275, 162
 Kaasalainen M., Binney J., 1994, MNRAS, 268, 1033
 Laskar J., 1993, CeMDA, 56, 191
 Lynden-Bell D., 1962, MNRAS, 124, 95
 Matthias M., Gerhard O.E., 1999, MNRAS, in press
 McGill C., Binney J., 1990, MNRAS, 244, 634
 Miralda-Escudé J., Schwarzschild M., 1989, ApJ, 339, 752
 Ollongren A., 1962, BAN, 16, 241
 Papaphilippou Y., Laskar J., 1996, A&A, 307, 427
 Papaphilippou Y., Laskar J., 1998, A&A, 329, 451

Ratcliff S. J., Chang K. M., Schwarzschild M., 1984, ApJ, 279, 610
 Richstone D. O., 1982, ApJ, 252, 496
 Rix H. W., de Zeeuw P. T., Cretton N., van der Marel R. P., Carollo C. M., 1997, ApJ, 488, 702
 Saaf A. F., 1968, ApJ, 154, 483
 Schwarzschild M., 1979, ApJ, 232, 236
 Sridhar S., Touma J., 1997, MNRAS, 287, L1 (ST)
 Valluri M., Merritt D., 1998, ApJ, 506, 686
 Zhao H. S., 1996, MNRAS, 283, 149

APPENDIX A: SRIDHAR & TOUMA POTENTIAL

The test-orbit used in §4.1 was integrated in the two-dimensional separable potential introduced by Sridhar & Touma (1997, ST). We collect here a number of properties of the orbits in this potential.

The ST potential is defined by

$$\Phi(r, \theta) \hat{=} r^\alpha \left[(1 + \cos \theta)^{(1+\alpha)} + (1 - \cos \theta)^{(1+\alpha)} \right]. \quad (\text{A1})$$

It is of Stäckel form in parabolic coordinates $\xi = r(\cos \theta + 1) \geq 0$ and $\eta = r(\cos \theta - 1) \leq 0$, in which it takes the form

$$\Phi = \frac{F_+(\xi)}{\xi - \eta} + \frac{F_-(\eta)}{\eta - \xi}, \quad (\text{A2})$$

with $F_+(\xi) \hat{=} 2\xi^{1+\alpha}$ and $F_-(\eta) \hat{=} -2|\eta|^{1+\alpha}$.

In addition to the energy

$$E = \frac{2}{\xi - \eta} (\xi p_\xi^2 - \eta p_\eta^2) + \Phi, \quad (\text{A3})$$

every orbit has a second isolating integral of motion I_2 , given by

$$I_2 = 2\xi p_\xi^2 - \xi E + F_+(\xi) = 2\eta p_\eta^2 - \eta E + F_-(\eta). \quad (\text{A4})$$

As eq. (A1) shows, the ST potential is scale-free, so that the shape of an orbit is determined only by the value of the second integral, while its scale is related to the energy. Two orbits of opposite I_2 are symmetric with respect to the x -axis; we consider hereafter only the case $I_2 \geq 0$.

Defining the functions $I_+(\eta) \hat{=} -\eta E + F_-(\eta)$ and $I_-(\xi) \hat{=} -\xi E + F_+(\xi)$ for a given energy E , the boundaries of an orbit with second integral I_2 (≥ 0) are given by the roots of the equations $I_+(\eta) = I_2$ (2 roots η_1 and η_2) and $I_-(\xi) = I_2$ (one root ξ_0 ; see e.g., Fig. 3).

The orbital DF of an orbit with energy E_0 and second integral I_0 can be written (as a consequence of the strong Jeans theorem) as:

$$f_{E_0, I_0}(E, I_2) \propto \delta(E - E_0) \delta(I_2 - I_0). \quad (\text{A5})$$

The orbital surface density is as usually given by $\rho_{E_0, I_0}(r, \theta) \hat{=} \int f_{E_0, I_0} d^2v$. We have $d\xi d\eta dp_\xi dp_\eta = dr dv$, which translates to:

$$d^2v = \frac{1}{r} \frac{\partial(\xi, \eta)}{\partial(r, \theta)} \frac{\partial(p_\xi, p_\eta)}{\partial(E, I_2)} dE dI_2, \quad (\text{A6})$$

with

$$\frac{\partial(\xi, \eta)}{\partial(r, \theta)} = 2r \sin \theta, \quad (\text{A7})$$

and

$$\frac{\partial(p_\xi, p_\eta)}{\partial(E, I_2)} = \frac{1}{2} \frac{1}{\sqrt{(I_+(\eta) - I_0)(I_0 - I_-(\xi))}}. \quad (\text{A8})$$

Therefore, the unnormalized orbital density ρ^* is

$$\rho_{E_0, I_0}^*(\xi, \eta) = \frac{1}{2} \frac{1}{\sqrt{(I_+(\eta) - I_0)(I_0 - I_-(\xi))}}, \quad (\text{A9})$$

while the total mass of this unnormalized orbit is found to be:

$$M_{E_0, I_0}^* \hat{=} \int \rho_{E_0, I_0}^* d^2r \quad (\text{A10})$$

$$= \frac{1}{4} \left[\int_{\eta_1}^{\eta_2} \frac{\sqrt{\eta}}{\sqrt{\delta_\eta}} d\eta \int_0^{\xi_0} \frac{d\xi}{\sqrt{\xi} \sqrt{\delta_\xi}} \right. \quad (\text{A11})$$

$$\left. + \int_{\eta_1}^{\eta_2} \frac{d\eta}{\sqrt{\eta} \sqrt{\delta_\eta}} \int_0^{\xi_0} \frac{\sqrt{\xi}}{\sqrt{\delta_\xi}} d\xi \right], \quad (\text{A12})$$

with shorthand notations $\delta_\eta \hat{=} I_+(\eta) - I_0$ and $\delta_\xi \hat{=} I_0 - I_-(\xi)$. This double integration can be carried out easily by numerical means.